

Controlled nucleation in methylamine-treated perovskite films by artificial seeding and phase-field simulations

November 27, 2025

Emilia R. Schütz^{a†}, Martin Majewski^{b†}, Olivier J.J. Ronsin^b, Jens Harting^{b,c*}, Lukas Schmidt-Mende^{a*}

a) Department of Physics, University of Konstanz, Universitätsstraße 10, Konstanz, 78464, Germany

b) Helmholtz Institute Erlangen-Nürnberg for Renewable Energy (HIERN), Forschungszentrum Jülich GmbH

c) Department of Chemical and Biological Engineering and Department of Physics, Friedrich-Alexander-Universität Erlangen-Nürnberg, Fürther Straße 248, Nürnberg

† These authors contributed equally to this work.

Email Address: j.harting@fz-juelich.de, lukas.schmidt-mende@uni-konstanz.de

Abstract

Large perovskite crystals with reduced defect density enable superior charge transport and stability. Therefore, controlling their nucleation and growth is key to advancing high-performance optoelectronic devices based on perovskite semiconductors. Millimeter-scale perovskite crystals can be synthesized as a continuous film through methylamine treatment, with nucleation sites directed by pre-patterned seeds. Nonetheless, certain configurations may lead to unwanted parasitic nucleation. To predict and mitigate this effect, we employ phase-field simulations alongside an analytical model. Their predictive capability is demonstrated across three distinct material-substrate systems, enabling precise control over nucleation and subsequent crystal growth. Notably, the only material-specific input required is the nucleation density (i.e., the number of crystals nucleated per unit area on an unpatterned substrate). This generality makes the models broadly applicable to diverse material systems for achieving controlled two-dimensional crystallization for improved optoelectronic device performance. keywords: methylamine treatment, seeded growth, PF simulation, analytical model

1 Introduction

Perovskite materials attracted significant attention in recent years due to their remarkable optoelectronic properties [1]. The formation of large perovskite crystals, ideally to single-crystalline devices, is considered highly desirable, as it reduces defects at grain boundaries [2] and enhances the stability of the material [3]. These characteristics are crucial for improving the performance and longevity of perovskite-based devices.

An effective method to achieve large grain sizes in perovskite films is through methylamine treatment. Through the reaction between methylamine gas and the perovskite material, an existing film can be dissolved and recrystallized with altered properties that are determined only by this single treatment step [4]. As the original film quality is not decisive for the final film properties, this treatment potentially eliminates the need for meticulous optimization of earlier steps. In addition, it enables straightforward

upscaling by facilitating large-scale fabrication without demanding high precision in the initial film deposition. Crucially, the method can be used to slow down a nucleation and growth process, producing exceptionally large grains that are beneficial for applications in solar cells [5, 6] and photodetectors [7]. The ability to pattern substrates with artificial nuclei offers further control over the crystallization process, allowing for the pre-determination of grain size, position, and orientation [8, 9]. This level of control could be particularly advantageous for applications requiring high crystallinity and precise structural organization, such as in LEDs, laser devices, and lateral perovskite devices such as back-contacted solar cells. Moreover, patterned growth enables us to create interesting model systems to deepen our understanding of the crystallization process itself.

Controlled two-dimensional growth has been explored in various material systems, and its broader implications extend beyond perovskites [10, 11, 12, 13, 14]. The ability to grow highly crystalline elements directly on circuit structures with controlled properties opens up possibilities for numerous technological applications. However, despite its potential, there has been limited research into understanding and simulating these types of growth processes. Much of the current knowledge is based on trial and error, underscoring the need for a more systematic investigation into the limitations and capabilities of patterned growth techniques.

To go beyond trial and error, a theoretical description of the underlying processes is required. Phase-field (PF) simulations offer an attractive approach to this problem, since they can numerically describe the phase change from amorphous to solid [15, 16, 17]. PF models are coarse-grained models with diffuse interfaces, based on the minimization of a free energy. The phenomenon of nucleation can be included in PF models by applying fluctuations on the evolution equation [18]. By including this effect, heterogeneous nucleation and crystal growth in confined spaces have been investigated [19]. The solution processing of perovskite systems has been investigated by studying the interplay of solvent evaporation and crystal growth [20] and furthermore including nucleation [21, 22]. Nevertheless, to the best of our knowledge, the presence of seed crystals in the initial state and allowing additionally for spontaneous nucleation has not been investigated in the literature so far.

In this work, two of these models, a phase field simulation and an analytical model, are used to optimize the experimental patterning of a methylamine-treated perovskite thin film. The main problem with patterning is the appearance of 'parasitic' crystals at spots which are not intended by the patterning. We recover this behavior with PF simulations [23], where we place crystals in the initial state in an hexagonal lattice and allow for additional nucleation. Based on the simulations, we propose an analytical model describing this behavior. Our models show that the main criteria for the appearance of parasitic crystals is an dimensionless parameter, calculated from the distance between the seeds and the nucleation density. Consequently, we predict this distance depending only on the nucleation density of the system. Hence, we are able to evaluate the feasibility of any arrangement of seeds to fully control the nucleation and growth process and avoid parasitic crystallization.

The paper is structured as follows: First, we introduce the methylamine treatment and the patterning processes. Then, we describe the theoretical results including the phase-field simulations, the derivation of the analytical model, and the validation of the predictions for three different experimental systems. Finally, the generality of the models is discussed before we conclude with a summary of our finding.

2 Methylamine treatment process

The methylamine post-treatment we apply in this work is a versatile instrument in modifying perovskite thin films [4] and achieving up to millimeter-sized grains [5, 7]. It allows us to achieve controlled, very slow nucleation and crystallization, yielding a compelling model system to observe growth mechanisms. The full treatment process is shown in Figure 1 a). It is based on the reaction between methylamine gas and the perovskite lattice: The amine replaces the Pb-I bonds due to its proclivity to coordinate Pb^{2+} [24]. Consequently, the perovskite lattice collapses into a liquid intermediate state, with the methylamine acting essentially as a gas-phase solvent [25]:



Once the methylamine leaves the film, inducing a state of supersaturation, the perovskite phase recrystallizes. In Figure 1 b), the phase diagram of this system is shown. Experimentally, we achieve liquefaction or recrystallization by changing the system temperature T and the methylamine partial pressure p_{MA} . Figure 1 c) shows the nucleation and recrystallization process, as observed in-situ. Grains nucleate at

random points, then grow outward until they cover the entire surface. For a more detailed explanation of the treatment process, see [7].

During this process, the exact grain location, i.e., the points of nucleation, remain functionally random, as they are likely to be determined by impurities or protrusions on the substrate. To gain complete control over the final film, we thus introduce artificial seeds onto the substrate.

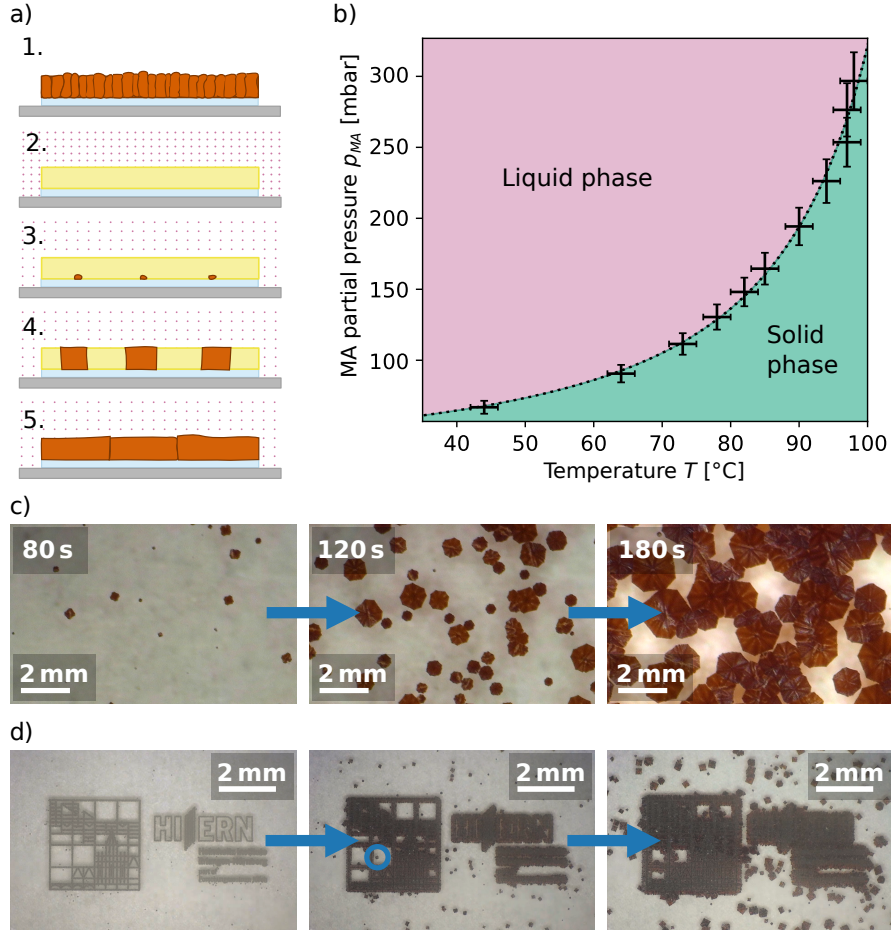


Figure 1: a) Schematic of the methylamine treatment process. b) Phase diagram of the methylamine process: For sufficiently high methylamine (MA) partial pressures p_{MA} at sufficiently low temperatures T , the system enters a liquid intermediate state. Through a reduction in p_{MA} , the system is brought just across the phase boundary, where slow nucleation and recrystallization ensues. The quantitative values presented here were derived for triple cation perovskite on an ITO substrate. c) Images of a sample during recrystallization. d) Images of the successful artificial nucleation of the perovskite. Note that the underlying Au structure is not visible, only the resulting perovskite crystals. Where the nucleating structures are too far apart, additional 'parasitic' nuclei grow (an example is circled in blue).

2.1 Gold patterning for nucleation control

Generally, nucleation most likely occurs heterogeneously at the substrate/liquid interface, and the likelihood of nucleation is highly sensitive to the substrate material. Gold has been found to be an effective seed material for various substances [26, 27], including perovskites [8]. By using lithographically patterned gold dots as nucleation centers, we can thus create preferred points for nucleation on our substrate. By carefully selecting the recrystallization parameters, the temperature T and the methylamine partial

pressure p_{MA} , we maintain a state of supersaturation that prevents nucleation at the substrate interface but allows for it at the gold sites. This enables us to effectively control the precise arrangement of grains in the film. For a more detailed explanation of the nucleation control mechanism, see the Supplementary Information, section S1. In Figure 1 d), the controlled nucleation and growth on the gold patterned substrate is shown.

While this scheme delivers the controlled growth of large-grained perovskite structures, there are limits to the seed pitch at which this process works well: As there is a remaining nucleation probability at the substrate interface, parasitic nucleation is observed between the artificial seeds above a certain seed distance D_{max} (see the features circled in blue in Figure 1 d)). The extend to which unwanted, parasitic, grains appear is of great importance for future applications: D_{max} effectively limits the size of any circuit or device into which the grown grains are to be integrated. This question does not only pertain to this specific material system, but to all 2D nucleation systems, in some of which parasitic grain formation is also clearly visible [10]. In the following, we approach this problem from a theoretical perspective by using phase-field simulations and constructing an analytical model.

3 Results

3.1 Phase Field predictions for the maximal seeding distance

In this chapter phase-field (PF) simulations are presented. The equations governing the simulation have been published [23] and are described in the Supplementary Information, section S2. A two-dimensional top view of the system with periodic boundary conditions in both directions. The initial amorphous material transforms to the crystalline phase with the system's evolution described using an order parameter. To allow for handling multiple crystals, each crystal is uniquely labeled with a marker field. Nucleation is triggered by thermal fluctuations of the order parameter.

To mimic the gold patterning of the substrate, the initial state of the simulation features round crystals positioned in a hexagonal lattice. Like in the experiments, we vary the distance between the seed crystals. Ten different simulations are performed for each pitch, and the number of parasitic grains is recorded. The resulting number of parasitic crystals depends on the nucleation rate κ and the growth rate of the nucleated crystals v_g . These quantities depend on the combination of material and substrate. However, they are often unknown and difficult to measure experimentally. To connect the simulation results to experimental systems, we scale the results to the final crystal density η on an unpatterned substrate:

$$\eta = \frac{\text{Number of crystals}}{\text{Area}}. \quad (2)$$

η depends on crystal surface tension κ and crystal growth speed v_g , and is (relatively) easily accessible experimentally. The final results depend only on this single material property and the pitch D , which allows for the comparison between simulation and experiments.

The number of parasitic crystals N , averaged over 10 simulation runs and scaled by the number of initial seeds, is shown in Figure 2. As described above, the pitch is scaled with the square root of the nucleation density η . We observe that there is a range of small pitches, up to $D\sqrt{\eta} = 0.5$, where (nearly) no parasitic nucleation occurs. Interestingly, exactly no parasitic nucleation occurs only for smaller values up to $D\sqrt{\eta} = 0.25$. Above $D\sqrt{\eta} = 0.5$, the number of parasitic grains increases. The results are robust against changes in the sizes of the seed crystals and lattice arrangement (see Supplementary Information, sections S2.5 and S2.6). To gain a more fundamental insight into the number of parasitic grains, we develop an analytical model of the process in the following section.

3.2 Analytical model

In order to derive the model, we consider a single triangle of crystals. This represents the basic unit of the hexagonal lattice used in the experiments. The appearing crystals have an initial size of $r_0 = 0$ and growth with a speed of v_g . An amorphous precursor phase is present between the crystals. In the amorphous phase, the nucleation rate is κ , which is assumed to be constant in time and space. The number of parasitic grains N can be calculated by

$$N = \int_0^\infty \kappa A(t), \quad (3)$$

where $A(t)$ is the surface which is not crystallized at time t . When crystals are placed initially, $A(t)$ has to account for the growth of these crystals. For simplicity, we neglect the effect of parasitic crystals

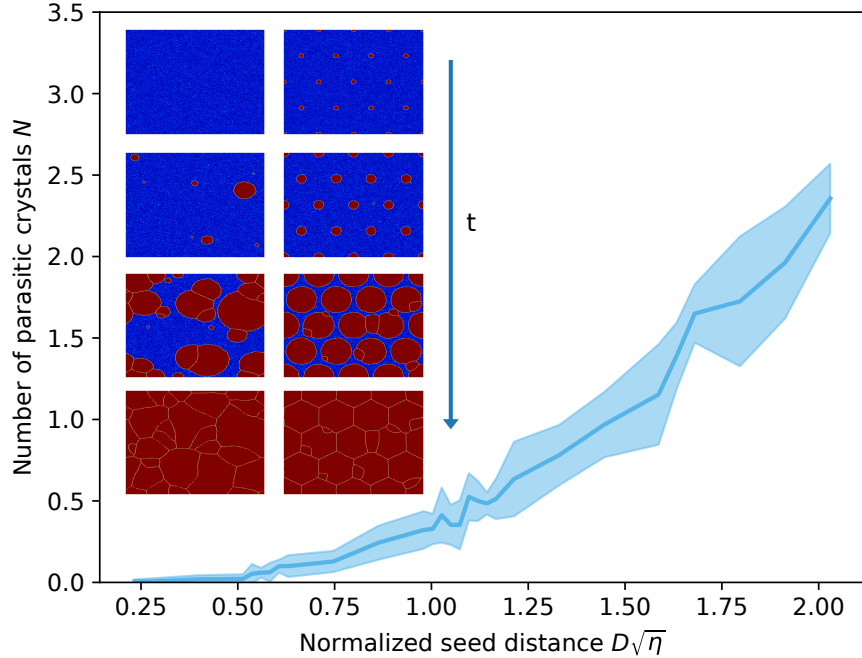


Figure 2: The average number of parasitic crystals in dependence on the pitch D . The shaded area depicts the standard deviation over 10 simulation runs. Note that the only difference between the simulations, for the same pitch, is the random fluctuations. Insets: Snapshots of the time evolution of a substrate without (left) or with (right) initial seed crystals in the simulation. The amorphous phase is depicted in blue, and the crystalline phase is shown in red.

on the available volume for crystallization. This will lead to an overestimation of crystals for large seed distances. We expect to have a nucleation induction time t_0 , which is the time between the start of crystal growth and the first nucleation event. Since the crystal growth of the seeds will result in full coverage of the available space within a finite time, the upper integration limit can be set to a finite value. This results in (derivation in the Supplementary Information, section S3)

$$N = \frac{\kappa I^3}{4v_g} \left(1 - \frac{\pi}{12}\right) + \frac{\kappa I^2 t_0}{2} \left(\frac{t_0^2 v_g^2}{3} - 1\right), \quad (4)$$

where I is a parameter in the integration limit. A lower limit for the number of parasitic crystals can be set, if $I = D$. At this point, the initial crystals will first touch, but do not cover the entire space. An upper limit can be determined by using the time it takes for the seed crystals to cover the entire available space, $I = 1.15D$. In this case, parts of the system are considered twice, resulting in an overestimation of the number of crystals. The limits are sketched in the inset in Figure 3. v_g, κ, t_0 and η can be measured from a PF simulation of nucleation on a bare substrate (see Supplementary Information, section S3.1). In principle, η could be calculated from the nucleation rate κ and the growth rate of the nucleated crystals v_g . However, nucleation models are not precise enough to estimate the crystal density (see Supplementary Information, section S3.2). Therefore, η is extracted from the simulations.

The results of the analytical model are plotted on top of the simulation results in Figure 3. The two curves overlap. Note that with this set of parameters, the impact of the nucleation induction time is comparatively small.

3.3 Experimental verification for different nucleation densities

Both model and simulation are capable of describing the problem at hand with remarkable generality; the only system specific parameter to the material system is the nucleation density η observed on a substrate without seeds. To validate the theoretical results, we therefore choose different model systems

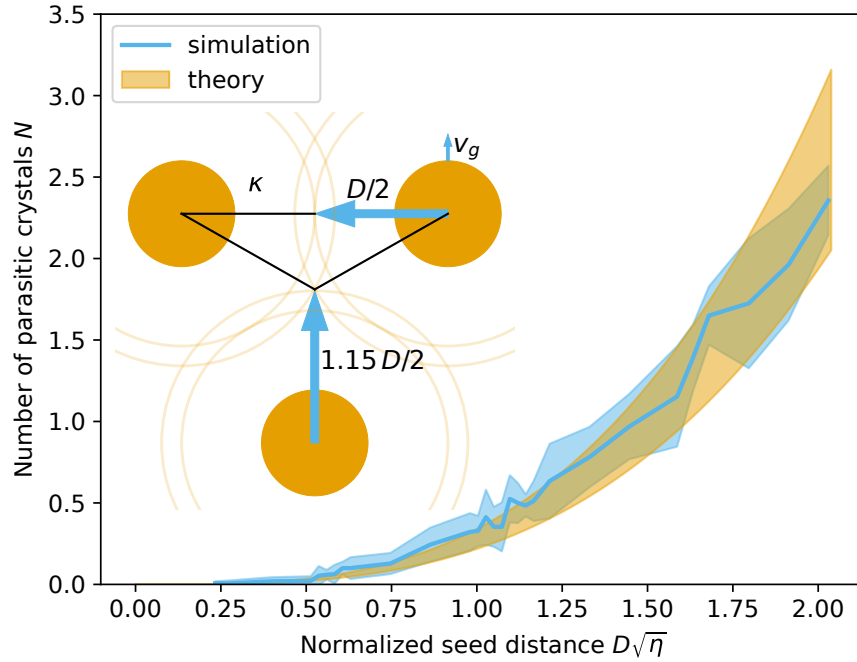


Figure 3: The number of parasitic crystals obtained from the simulation and calculated analytically (Equation 4). Inset: sketch visualizing the parameters of the analytical model. The three crystals (orange) represent an unit cell of the hexagonal lattice. The crystals grow with a growth speed of v_g , while additional crystals nucleate in the amorphous phase with a rate of κ . The arrows and shaded circles visualize the lower and upper integration limits of the model (see main text).

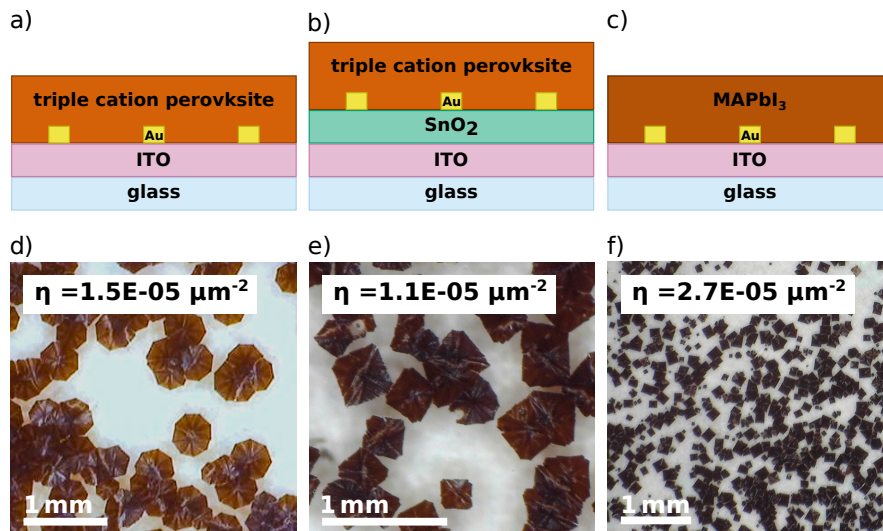


Figure 4: Different experimental stacks a), b), c), and directly below the experimental results during recrystallization on unpatterned substrates d), e), f). The different material systems result in different nucleation densities η .

which feature different values of η .

Within the experimental setup described in section 2, there are several ways to modify η . A possible approach is to vary the atmospheric treatment conditions T and p_{MA} : By having the system recrystallize in a more or less pronounced state of supersaturation, the nucleation probability, and thus density, can be shifted substantially. The closer to the phase boundary the system lies in the end, the smaller the nucleation rate, and hence the nucleation density.

Another approach is to vary the material system: The specific substrate/perovskite combination determines the interfacial energy in the liquefied state, thus changing the likelihood of heterogeneous nucleation. In addition, impurities and roughness at a given substrate surface impact the density of potential nucleation sites, in turn influencing the density of stable nuclei.

To demonstrate the generality of the models presented in section 3.1 and 3.2, we choose to investigate three different combinations of perovskite composition and substrate material, shown in Figure 4 a), b), and c), which are chosen strategically to cover a large range of nucleation densities η . Two different perovskite compositions are studied: MAPbI₃ and the triple cation perovskite Cs_{0.1}(MA_{0.17}FA_{0.83})_{0.9}-Pb(I_{0.83}Br_{0.17})₃. Both are deposited on ITO glass, and the triple cation perovskite is additionally studied on a SnO₂ substrate.

To perform a seeded growth analysis within the framework of the model presented in section 3.1 and 3.2, the native nucleation densities η have to be extracted for each of the systems. Equivalent to the extraction of η from the phase-field simulations in section 3.1, we fabricate films on bare substrates without artificial nucleation centers and let them recrystallize under the same conditions later chosen for the seeded growth. Through in-situ microscopic observation of the recrystallization process, the location of each new grain is recorded, thus yielding the values for η through a sequential image analysis further described in the methods section. Images of the films during recrystallization are shown in Figure 4 d), e), and f). The resulting values for η are $1.1 \times 10^{-5} \mu\text{m}^{-2}$, $1.5 \times 10^{-5} \mu\text{m}^{-2}$ and $2.7 \times 10^{-5} \mu\text{m}^{-2}$. Based on these values, samples with Au seeds arranged in hexagonal patterns with different distances D are fabricated and analyzed. The selected seed distances D for each system are chosen to cover a range of $D\sqrt{\eta}$ matching the theoretical data in Figure 3. The recrystallization process is observed in-situ. Sequential image analysis (further described in the Supplementary Information, section S4) yields the total number of nuclei appearing in the observed area. From there, the number of additional grains per artificial seed is extracted, equivalent to the simulated data in section 3.1.

The resulting values are shown in Figure 5. The experimental results are in good agreement with both simulation and the analytical model. The error bars shown represent the standard deviations of the resulting values for all evaluated samples for this pitch.

Note that, for very low pitches, sometimes fewer grains nucleate than seeds are present on the substrate: In contrast to the simulation, where crystals are placed at these spots initially, nucleation does not occur at all seeds simultaneously. It may occur that a grain nucleates and overgrows the neighboring seeds before nucleation has happened there. In that case not every seed will lead to a separate grain. This occasionally gives rise to a negative number of parasitic grains at the low $D\sqrt{\eta}$.

Furthermore, the size of the gold seeds has to be considered carefully. If the critical radius for nucleation is smaller than the seeding spot, multiple nucleation events may happen at a single seed. This behavior can be observed for some crystals in Figure 6 d). It will ultimately not impact the growth dynamic itself, and be very hard to recognize in the final film, but a 'grain' started like this will consist of at least two separate crystalline domains.

Despite these differences, the model predicts the experiments remarkably well, as is visually shown in Figure 6. Both in the experiments and the simulations, the underlying hexagonal seed pattern is clearly visible. For higher pitches D , where $D\sqrt{\eta} \approx 1.2$ (see Figure 6 a) and b), some parasitic nucleation in between the predetermined spots occurs, while that is not the case for the lower pitches shown in Figure 6 c) and d).

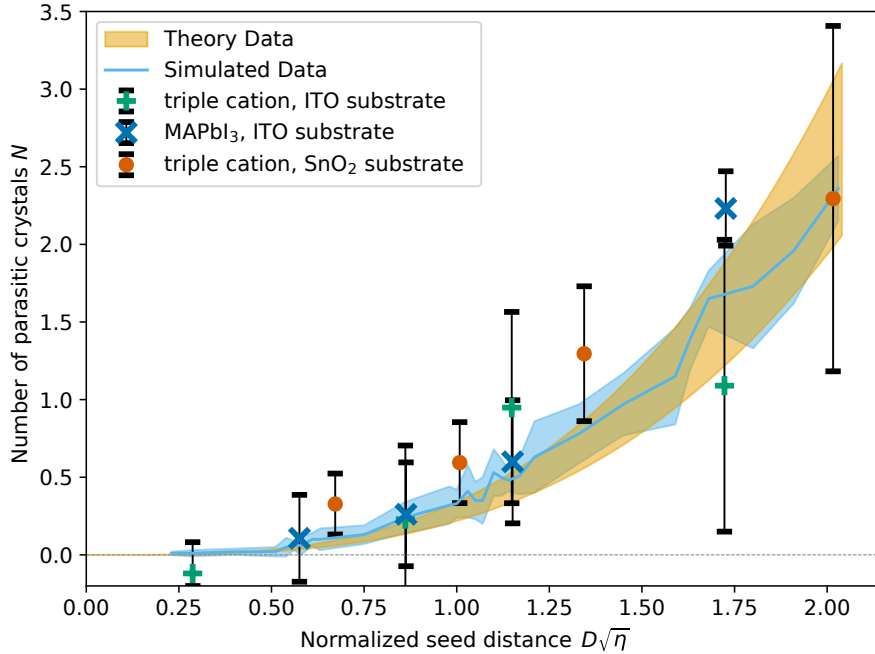


Figure 5: Experimental results of the number of excess grains over $D\sqrt{\eta}$ for the three material systems, along with the simulation data and analytical model curves. The experimental results match the theoretical data. The numbers shown here are the mean values derived from multiple growth processes and image analyses. The error bars correspond to the standard deviation of these values. The values result from the analysis of between 6 and 15 image sequences per data point, where each image series tracks one recrystallization process. For more details, reference the methods.

4 Discussion

The only system specific parameter used in the model is η which can be used to adjust the results to a wide range of length scales and defines the possible seed arrangements. η exists for any material system and is not exclusive for perovskite systems, hence the prediction should hold for any material system. Our experiments with different nucleation to growth rate ratios have already shown this flexibility for perovskites. Hence, we postulate that, as long as a continuous film is formed by nearly-isotropic 2D growth of the crystals, our model is able to predict viable distances.

One can, of course, conceive several possible extensions that would open the model to even broader application (see Supplementary Information, section S5). In its present form, the model already possesses the capability to significantly contribute to the advancement of strategic, highly optimized electronic- and optoelectronic devices. In applications and devices where the crystallographic direction and the relative position of grain boundaries are relevant, the model presented here can be used to evaluate possible layouts and to predict limitations of the system in question: For example, if crystals are to be grown across a gap between electrodes (i.e. in transistors [14, 28], or photodetectors [29]), we can predict how far apart these electrodes and the nucleation structures can be to ensure single-grain growth as intended. This idea can be expanded to nearly all applications where crystals are grown directly onto a functional structure, and where the location, crystallinity, and orientation of the crystal is of importance. That opens up a large field of research to be explored: At the moment, seeded 2D growth is frequently done from the vapor phase through epitaxy [12, 13] or vapor deposition [11]. Solution-based methods are, however, easy to scale up and would be easily integrated in already-established fabrication protocols. Using the understanding and the model we propose here will aid in the systematic planning of experiments and fabrication strategies. Consequently, this work could aid in expanding on this field in a way that would be highly interesting for industrial production.

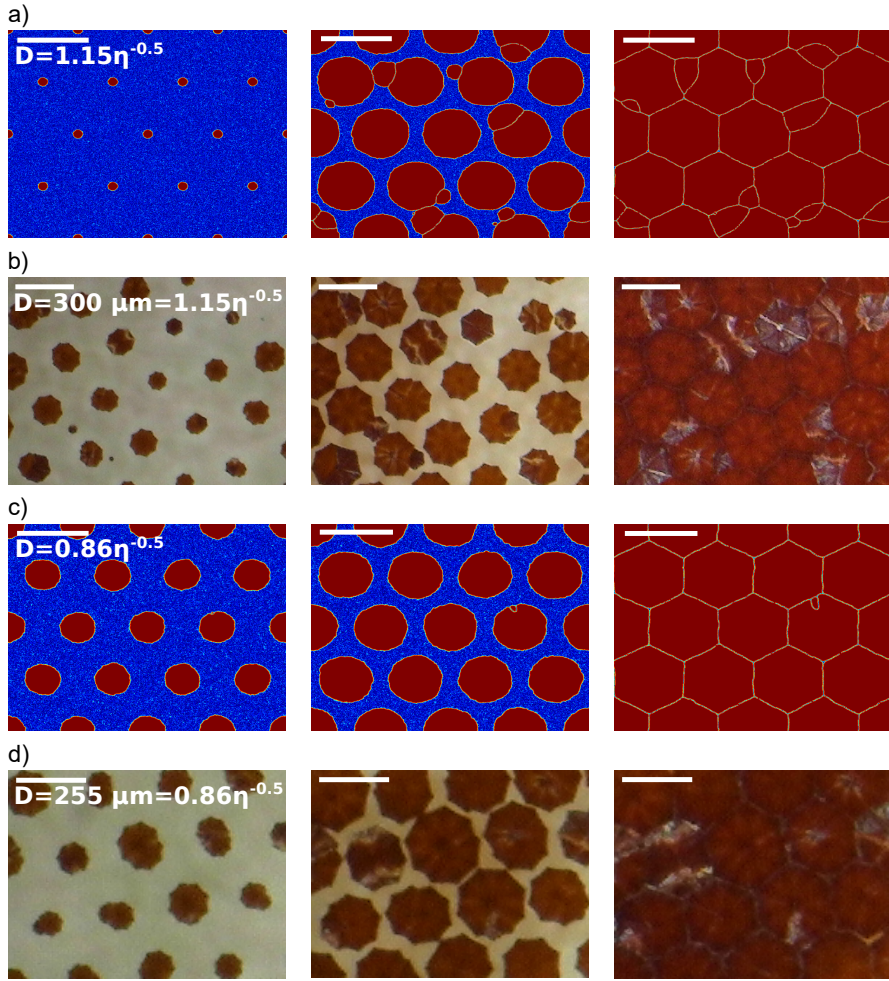


Figure 6: Simulated growth a) and experiment b) for large seed pitches D that lead to the formation of surplus grains. In contrast, c) and d) show simulation and an experiment for smaller D , where only the intended grains grow. The temporal progression is shown from left to right. The bright spots and lines seen in the experimental images on the crystals are caused by light reflections.

5 Conclusion

Millimeter-sized grains can be created with the methylamine treatment process. By adding gold seeds onto the substrate, the spots of nucleation for new grains can be controlled, allowing for full control of size and shape of the crystal. However, parasitic nucleation may occur during this process, potentially spoiling the quality of the final film. To better understand this phenomenon, the system was simulated using a phase-field simulation and an analytical model was developed. These models can predict the occurrence of parasitic nucleation and have been successfully validated against experiments with three different substrate-perovskite material combinations. We find that the value of a dimensionless number, comparing the distance between the seeds and the density of crystals nucleated on a bare substrate defines the occurrence of parasitic nucleation. The prediction of the model is unaffected by the kind of material, the length scale of the system, and the nucleation to growth rate ratio, making it very flexible in its application. Consequently, these models can be utilized for the systematic optimization of nucleation patterns in controlled 2D crystallization as demonstrated here with perovskite films.

Supplementary information

Simulation data is publicly available via <https://doi.org/10.5281/zenodo.17200698>. The remaining data that support the findings of this study are included in the supplementary information or available from the corresponding authors upon reasonable request.

Acknowledgements

We acknowledge financial support from the Deutsche Forschungsgemeinschaft (DFG) via the Perovskite SPP2196 programme (Projects No. 506698391 and No. 423660474), the European Commission (H2020 Program, Project 101008701/EMERGE), and CRC1719 Chemprint (Project No. 538767711).

Conflicts of interest

The authors declare no conflict of interest.

Authors Contributions

E. S. and M. M. conceived the idea. E. S., M. M., L. S. M., O. R., J. H. designed the project. L. S. M., O. R., J. H. supervised the project. E. S. fabricated the samples and carried out the characterizations. M. M. performed the PF simulations and created the analytical model. E. S. and M. M. wrote the text of the manuscript. L. S. M., O. R., J. H. revised the manuscript. All authors contributed to the discussion and commented on the manuscript.

6 Methods

6.1 Sample preparation

Samples are prepared on ITO glass substrates (Luminescence Technology Corp., $15\ \Omega$). After four 30 min-long steps of ultrasonication (deionized water with detergent, pure deionized water, Acetone, and Iso-propanol), the samples are subjected to 7 min of oxygen plasma treatment.

For the samples with a SnO_2 layer as growth interface, a SnO_2 nanoparticle suspension (Alfa Aesar, diluted 1 mL:4.612 mL in deionized water) is spin-coated at 3000 rpm for 30 s, followed by 30 min annealing at $120\ ^\circ\text{C}$.

Samples are then patterned with the Au seeds. After spin-coating an adhesive layer (TI Prime, Microchemicals) at 0 rpm for 0 s and a 2 min annealing step at $120\ ^\circ\text{C}$, a roughly 1000 nm thick photoresist (AZ MIR 701 (14 CPS), Microchemicals) layer is spin-coated at for and is baked for 90 s at $90\ ^\circ\text{C}$. Illumination of the resist is performed using laser lithography at a dose of $250\ \text{mJ cm}^{-2}$. After illumination and a 90 s bake at $120\ ^\circ\text{C}$, the resist is developed for 60 s (AZ 726 MIF, Microchemicals). After the thermal evaporation of 5 nm of Cr and 15 nm of Au, and a lift-off in Acetone, the samples are ready for perovskite deposition.

A 1.3 mol precursor of the triple cation perovskite is prepared in a N_2 -filled glovebox by dissolving 73.4 mg PbBr_2 (Sigma-Aldrich), 507.1 mg PbI_2 (TCI), 22.4 mg MABr (Greatcell Solar), and 172 mg FAI (Greatcell Solar) in a 4 : 1 mixture of DMF:DMSO and adding 53 μL of a $389.7\ \text{mg mL}^{-1}$ CsI (Sigma-Aldrich) solution in DMSO per mL of the solvent mixture. The finished precursor is filtered in a $0.45\ \mu\text{m}$ PTFE filter just before perovskite deposition. The perovskite layer itself is spin-coated in N_2 atmosphere. The precursor is dropped dynamically onto the spinning substrate at 1000 rpm. The sample is then sped up to 6000 rpm, where it remains for 25 s. 20 s into this faster step, 250 μL CB anti-solvent are dropped onto the substrate. Finally, the perovskite layer forms during a 40 min-long annealing step at $90\ ^\circ\text{C}$.

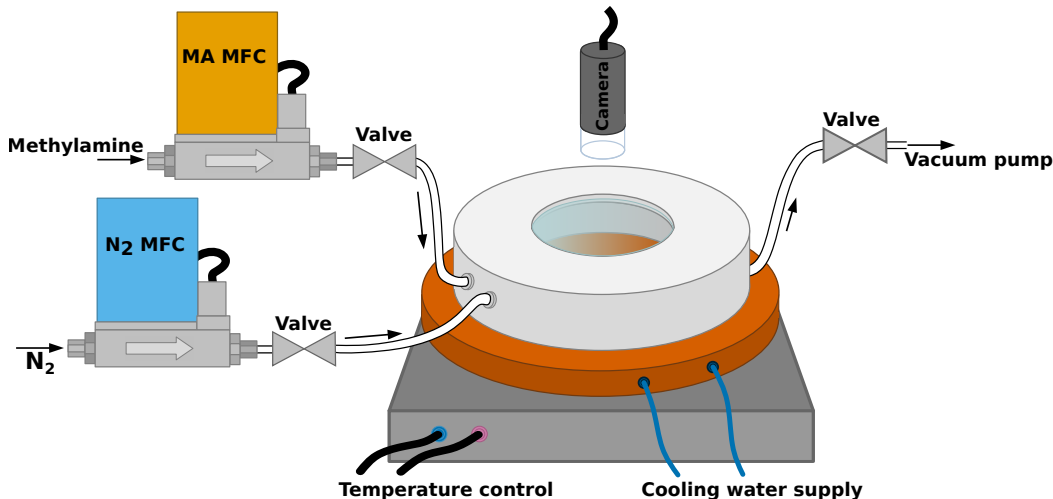


Figure 7: Schematic of the methylamine treatment setup. Two mass flow controllers are used to control the amount of N_2 and MA gas let into the chamber, which can be heated and cooled from below. A vacuum pump is used to pump to a specific pressure. The process can be observed with a microscope camera through a window of optical glass from the top.

6.2 Methylamine treatment setup

The as-prepared perovskite samples are subjected to methylamine (MA) gas (Linde) in a specially-built automated treatment chamber shown in Figure 7. The chamber can be heated to a specified temperature T with a thermoelement from below. It is equipped with two gas inlets (N_2 and MA) and one outlet, which is connected to a vacuum pump. The inlets are connected to mass flow controllers, allowing for

control over the precise amount N_{MA} of gas in the chamber. The total pressure in the chamber is set by pumping to a setpoint below atmosphere pressure p_{vac} with the vacuum pump. Methylamine partial pressures during exposure $p_{MA,1}$ are set by letting a specified amount of gas into the chamber (Volume V , temperature T):

$$p_{MA,1} = \frac{N_{MA} \cdot R \cdot T}{V} \quad (5)$$

with the molar gas constant R . The total pressure at this point amounts to $p_{tot,1} = p_{vac} + p_{MA,1}$. Recrystallization is induced by pumping the chamber down again to $p_{tot,2} = p_{vac}$, thus reducing the methylamine partial pressure $p_{MA,2}$ to:

$$p_{MA,2} = \frac{p_{tot,2}}{p_{tot,1}} \cdot p_{MA,1} = \frac{p_{vac}}{p_{vac} + p_{MA,1}} \cdot p_{MA,1}. \quad (6)$$

Through an optical glass window over the sample, the entire process is observed in-situ with a microscope camera (Dino-Lite).

The combinations of methylamine partial pressure $p_{MA,2}$ and temperature T are chosen in a way that ensures slow growth of grains and strong preferred nucleation at the Au seeds. The settings for all three experiments groups are shown in Table 1.

6.3 Image analysis and calculation of the number of parasitic crystals

During the recrystallization process, the sample is observed in-situ from above. From the resulting image material, the total number of nucleated grains N_{tot} in a given observed area A can be extracted. (See the SI for a detailed description of the sequential image analysis employed to that end.) To calculate the number of parasitic grains per artificial seed at a seed pitch D , equivalent to the simulated data shown in the paper, we normalize to the primitive hexagonal unit cell area $a = \sqrt{3}D^2/2$. The total number of grains in per unit cell n_{tot} is then calculated via

$$n_{tot} = \frac{a}{A} \cdot N_{tot}. \quad (7)$$

If we had nucleation exclusively at the artificial seeds, we would expect exactly one grain to nucleate in each unit cell. The number of parasitic grains N per unit cell is thus

$$N = \frac{a}{A} \cdot N_{tot} - 1. \quad (8)$$

Here, the fraction $\frac{a}{A}$ corresponds to the number of unit cells that fit into the observed area A , which is equivalent to the number of seeds in A , presuming one seed per unit cell.

In Table 2, the number of analyzed images sequences are shown for each combination of pitch and material system shown in Figure 5. Note that the values shown in Figure 5 result from the mean and standard deviation of all the values of N extracted for one parameter combination, weighted by the areas A that the analyzed images show for the different image sequences.

Note that the number of analyzed image sequences per experimental condition varies. For the smaller pitches in particular, some experiments failed due to contamination or other uncontrolled factors, resulting in fewer analyzable sequences.

Table 1: Recrystallization parameters for all three experimental groups. The precise combination of temperature T , methylamine partial pressure during recrystallization p_{MA} and substrate-liquid interaction determine the nucleation densities η on non-patterned substrates of each system.

Stack	T	p_{MA}	η
Glass/ITO/MAPbI ₃	70 °C	195 mbar	$2.7 \times 10^{-5} \mu\text{m}^{-2}$
Glass/ITO/3cat	85 °C	230 mbar	$1.5 \times 10^{-5} \mu\text{m}^{-2}$
Glass/ITO/SnO ₂ /3cat	80 °C	2.30 mbar	$1.1 \times 10^{-5} \mu\text{m}^{-2}$

Table 2: Number of image sequences analyzed for each combination of pitch and material system.

Stack	Pitch D	normalized Pitch $D\sqrt{\eta}$	Number of image sequences
Glass/ITO/MAPbI ₃	50 μm	0.168	8
Glass/ITO/MAPbI ₃	100 μm	0.336	5
Glass/ITO/MAPbI ₃	200 μm	0.672	15
Glass/ITO/MAPbI ₃	300 μm	1.008	12
Glass/ITO/MAPbI ₃	400 μm	1.344	9
Glass/ITO/MAPbI ₃	600 μm	2.016	12
Glass/ITO/MAPbI ₃	1000 μm	3.360	8
Glass/ITO/3cat	75 μm	0.287	8
Glass/ITO/3cat	150 μm	0.574	8
Glass/ITO/3cat	225 μm	0.861	15
Glass/ITO/3cat	300 μm	1.148	16
Glass/ITO/3cat	450 μm	1.723	8
Glass/ITO/3cat	750 μm	2.871	14
Glass/ITO/SnO ₂ /3cat	55 μm	0.288	6
Glass/ITO/SnO ₂ /3cat	110 μm	0.575	8
Glass/ITO/SnO ₂ /3cat	165 μm	0.863	8
Glass/ITO/SnO ₂ /3cat	220 μm	0.150	8
Glass/ITO/SnO ₂ /3cat	330 μm	0.173	6

6.4 Determination of phase transition temperatures

The phase transition points shown in the phase diagram in Figure 1 b) are experimentally determined for triple cation perovskite films. To achieve this, an untreated perovskite film is placed in the chamber and exposed to a defined amount of methylamine gas, corresponding to a methylamine partial pressure p_{MA} . This is repeated at increasing temperatures until the film does not liquefy anymore upon methylamine exposure. The corresponding temperature T is then noted as the transition temperature for the partial pressure p_{MA} in question.

The precision of the resulting values is limited by the accuracy of the set temperature and that of the set methylamine partial pressure, which is denoted in Figure 1 b) as error bars.

Supporting information of 'Controlled nucleation in methylamine-treated perovskite films by artificial seeding and phase-field simulations'

Emilia R. Schütz^{a†}, Martin Majewski^{b†}, Olivier J.J. Ronsin^b, Jens Harting^{b,c*}, Lukas Schmidt-Mende^{a*}

a) Department of Physics, University of Konstanz, Universitätsstraße 10, Konstanz, 78464, Germany

b) Helmholtz Institute Erlangen-Nürnberg for Renewable Energy (HIERN), Forschungszentrum Jülich GmbH

c) Department of Chemical and Biological Engineering and Department of Physics, Friedrich-Alexander-Universität Erlangen-Nürnberg, Fürther Straße 248, Nürnberg

† These authors contributed equally to this work.

Email Address: j.harting@fz-juelich.de, lukas.schmidt-mende@uni-konstanz.de

S1 Experimentally controlling nucleation during the methylamine treatment

In the phase diagram in Figure S8 a), the phase boundary between the solid and liquid states is shown based on experimentally measured data. Left of this curve, the film is liquid in equilibrium, while it is solid in equilibrium on the right side. When moving from the liquid state across the phase boundary, there is a range of temperature-pressure combinations where nucleation is unlikely to occur and the liquid state remains metastable. This metastable zone is bounded by the metastable limit curve (green line in Figure S8 a)), beyond which nucleation is likely to occur spontaneously.

The presence of the metastable zone and the position of the metastable limit can be understood from classical nucleation theory:

The formation of a nucleus is accompanied by a change in Gibbs free energy ΔG . This free energy change is comprised of a change in the volume free energy ΔG_v , and the surface free energy ΔG_s [30]:

$$\Delta G = \Delta G_v + \Delta G_s. \quad (\text{S9})$$

The volume free energy favors nucleation, as the solid phase is more energetically favorable in the region in question. It is the driving force of nucleation and can be expressed as

$$\Delta G_v = \frac{4}{3}\pi r^3 \Delta G_v^* \quad (\text{S10})$$

for a spherical nucleus of radius r . ΔG_v^* is the free energy difference between the liquid and solid state per unit volume. It depends on the degree of supersaturation S and the molecular volume v [30]:

$$\Delta G_v^* = -\frac{k_B \cdot T \cdot \ln(S)}{v} \quad (\text{S11})$$

The surface free energy ΔG_s is positive, as the formation of an interface between a solid phase and the liquid costs energy. For a spherical nucleus of radius r , it can be expressed as

$$\Delta G_s = 4\pi r^2 \gamma, \quad (\text{S12})$$

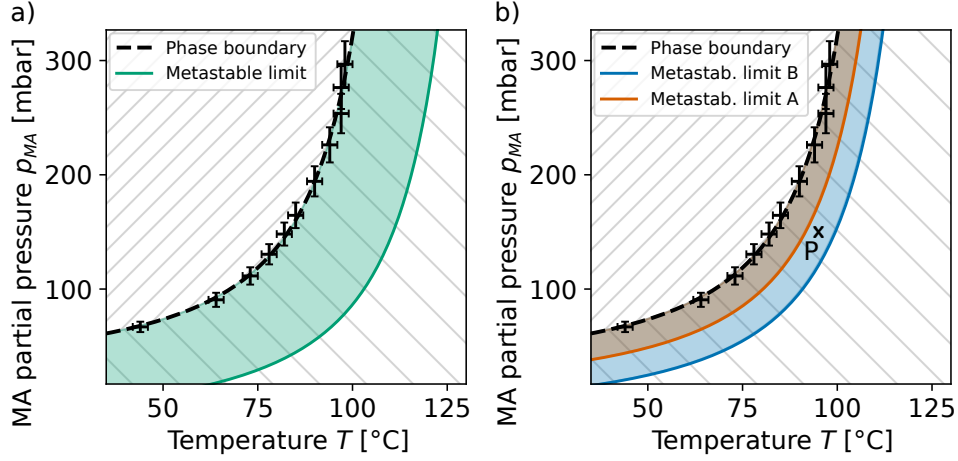


Figure S8: a) Phase diagram for the recrystallization process at hand, in case of homogeneous nucleation: beyond the phase boundary, a metastable zone exists (green), where nucleation is unlikely. b) Phase diagram and metastable zones from two different substrate materials that offer nucleation interfaces for heterogeneous nucleation. Depending on the specific interfacial energy with each material, the metastable zones will have different depths, leading to different nucleation probabilities for different materials. If crystallization is initialized at a point P , within the metastable zone for one material but not the other, nucleation can be suppressed at the surfaces of material B. Note that while the phase boundary displayed here consists of experimental data, the metastable limits are qualitative guides to the eye to illustrate the concepts involved and are not based on experimental data.

with the surface energy per unit area γ .

In Figure S9, ΔG is shown against r . If a nucleus overcomes the critical nucleus size r^* , it becomes stable and can grow into a grain. For that to happen, the energy barrier ΔG^* has to be overcome. By finding the maximum of Equation S9, using Equation S10 to Equation S12, this energy barrier can be expressed as [30]

$$\Delta G^* = \frac{16\pi \cdot \gamma^3}{3 \cdot (\Delta G_v^*)^2} \propto \gamma^3 \propto (\Delta G_v^*)^{-2}. \quad (\text{S13})$$

ΔG^* explains the existence of a metastable zone and dictates the position of the metastable limit curve. Within the metastable zone, this energy barrier prevents stable nuclei from forming. Furthermore, its dependence on ΔG_v^* directly implies an inverse dependence on the degree of supersaturation S . Moving away from the phase boundary, the supersaturation increases. Once ΔG^* is thus small enough for thermal fluctuations to overcome it, spontaneous nucleation can occur: the metastable limit is reached.

Thus far, we have only discussed homogeneous nucleation, which theoretically occurs in a medium without any impurities. The only interface, and thus the only interfacial energy of interest, is that between the liquid and solid state. However, in the thin-film system observed here, at least one other interface is possible: that with the substrate. In that case, heterogeneous nucleation occurs: nuclei form at the interface to a third material where the interfacial energy to the growing nucleus is smaller. That decreases the effective interfacial energy because the nucleus does not need to form a full spherical interface with the liquid phase: It instead forms a partial interface with (in our case) the substrate, which is energetically favorable. Due to the proportionality to γ^3 shown in Equation S13, this reduction of the effective interfacial energy decreases Gibbs free energy barrier, increasing the likelihood for nucleation.

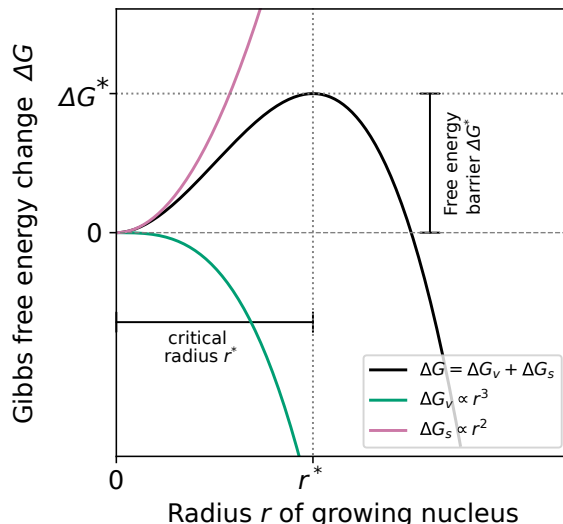


Figure S9: Gibbs free energy change ΔG for the formation of a spherical nucleus in dependence of the nucleus' radius r . The formation energy consists of a negative volume component and a positive surface component. The nucleus becomes stable above a critical radius r^* , when it has overcome the energy barrier ΔG^* .

Important to note here is that the *degree* to which the energy barrier decreases depends on the specific interfacial energies between the solid phase, the liquid and the substrate material. Different materials lead to different values of ΔG^* . In Figure S8 b), the implications for the resulting metastable zones are visualized qualitatively: Effectively, for two different materials, two different metastable limit curves arise. For the material of lower interfacial energy (in our case Au), the metastable zone is smaller, because there is a lower energy threshold to overcome for nucleation, and lower degrees of supersaturation suffice to achieve that. For the material of higher interfacial energy – in our case ITO – the metastable zone is larger.

This implies that by controlling p_{MA} and T carefully, we can choose conditions for recrystallization that lie within the metastable zone for nucleation at the ITO interface, but beyond the metastable limit for Au. We, thus, have a high probability for spontaneous nucleation *only* at the Au spots, while nucleation is suppressed everywhere else. For larger differences in interfacial energy, the gap between the two metastable limit curves is larger, making it easier to realize an effective nucleation control. Au seems to be particularly well-suited for that purpose [8], and we attribute that to a favorable interfacial energy between the growing nucleus and the Au surface. Finally, it is to be noted that while nucleation is unlikely within the metastable zone, it is not impossible. Additionally, impurities and structural inhomogeneities such as larger spikes on the ITO substrate create additional likely nucleation points on the substrates that are not fully accounted for here. Consequently, there is always a degree of spontaneous nucleation in between the seed structures, the limits and implications of which are this paper's central focus.

S2 Simulation Model

S2.1 Free Energy

The simulation code is based on [23]. The goal is to investigate crystal nucleation on a patterned substrate. Therefore, only the transition from an amorphous state to a crystalline state is of importance. The evolution of the system is tracked by a crystalline order parameter Φ , which is

zero in the amorphous state and becomes one in the crystalline state. To enable the simulation of a polycrystalline system, a so-called orientation parameter θ is recorded. This labelling field is used to distinguish the different crystals. The Gibbs free energy G is used to record the different energetic contributions:

$$G = \int_V dV \Delta G = \int_V dV G^{ls} + G^{interf}, \quad (\text{S14})$$

where G^{ls} describes the liquid-solid phase transition and G^{interf} the interfacial contributions. G^{ls} can be written as

$$G^{ls} = \rho (\Phi^2(3 - 2\Phi)L_{fus}(T/T_m - 1) + \Phi^2(\Phi - 1)^2W), \quad (\text{S15})$$

with ρ the density of the material, L_{fus} is the enthalpy of fusion, T the temperature, T_m the melting temperature, and W defines the height of the energy barrier upon liquid-solid phase change. The interfacial contribution G^{interf} can be written as

$$G^{interf} = \epsilon/2(\nabla\Phi)^2 + (3 - 2\Phi)\Phi^2\pi\epsilon_g\delta(\nabla\theta)/2, \quad (\text{S16})$$

where ϵ defines the contribution to the surface energy arising from the gradients in the crystalline order parameter, ϵ_g for the orientation parameter, and $\delta(\nabla\theta)$ is defined to be one if a difference in orientation is present and zero elsewhere.

S2.2 Dynamic Equation

The evolution of the system is given by the stochastic Allen-Cahn equation:

$$\frac{\partial\Phi}{\partial t} = -\frac{\nu_0}{RT}M \left(\frac{\partial\Delta G}{\partial\Phi} - \nabla \frac{\partial\Delta G}{\partial(\nabla\Phi)} \right) + d(\Phi, d_\chi, w_\chi, c_\chi)\chi, \quad (\text{S17})$$

where ν_0 is the molar volume, R the gas constant, M the mobility, d an interpolating function and χ fluctuations with zero mean and a second moment of

$$\langle \chi(x, t), \chi(x', t') \rangle = \frac{2\nu_0}{N_a} M \delta(t - t') \delta(x - x'), \quad (\text{S18})$$

with N_a being the Avogadro number. The interpolating function can be written as

$$\log(d(d_\chi, w_\chi, c_\chi)) = 0.5 \log(d_\chi) (1 + \tanh(w_\chi(\Phi - c_\chi))), \quad (\text{S19})$$

whose shape is defined by w_χ, d_χ, c_χ . The evolution of the orientation field is given as follows: If the crystalline order parameter rises above a certain threshold t_Φ , then we assign the orientation parameter of the nearest crystal or a new one, if no crystal is present nearby.

S2.3 Simulation Setup

The top view of the experiment is simulated. The two-dimensional simulation box has periodic boundary conditions. Sixteen crystals are initially placed in a triangular lattice. The setup is shown in Figure S10.

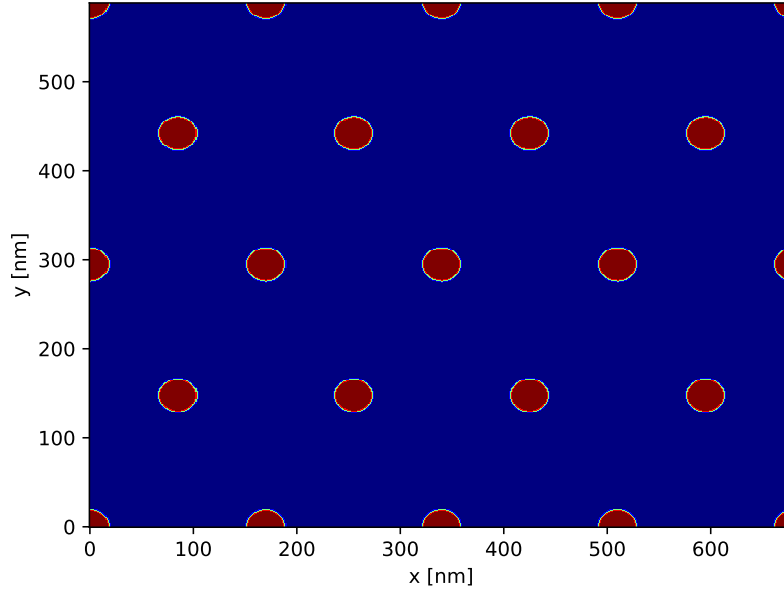


Figure S10: Simulation setup for pitch.

S2.4 Simulation Parameters

Table S3: Parameters of the simulations

Parameters	Full Name	Value	Unit
dx, dy	Grid spacing	1	nm
nx, ny	Grid size	varied	-
T	Temperature	460	K
ρ	Density	1000	kg/m^3
m	Molar mass	0.1	kg/mol
ν_0	Molar volume of the Flory Huggins lattice site	10^{-4}	m^3/mol
T_m	Melting temperature	600	K
L_{fus}	Heat of fusion	75789	J/kg
W	Energy barrier upon crystallization	142105	J/kg
P_0	Reference pressure	10^5	Pa
ϵ_c	Surface tension parameters for order parameter gradient	$1.4 \cdot 10^{-5}$	$(J/m)^{0.5}$
M_c	Allen Cahn mobility coefficient for the crystalline phase	48	s^{-1}
d_χ, c_χ, w_χ	Amplitude, center and width of the penalty function for the fluctuations	$10^{-2}, 0.85, 15$	-

S2.5 Nucleation to growth rate ratio

The influence of the nucleation-to-growth rate ratio is investigated. To this end, two sets of simulations are performed, varying the seed distance and the nucleation-to-growth rate ratio. As shown in Figure S11, this ratio leads to changes within the statistical uncertainties. The scaling with the nucleation density η on the x-axis is the reason for this behavior.

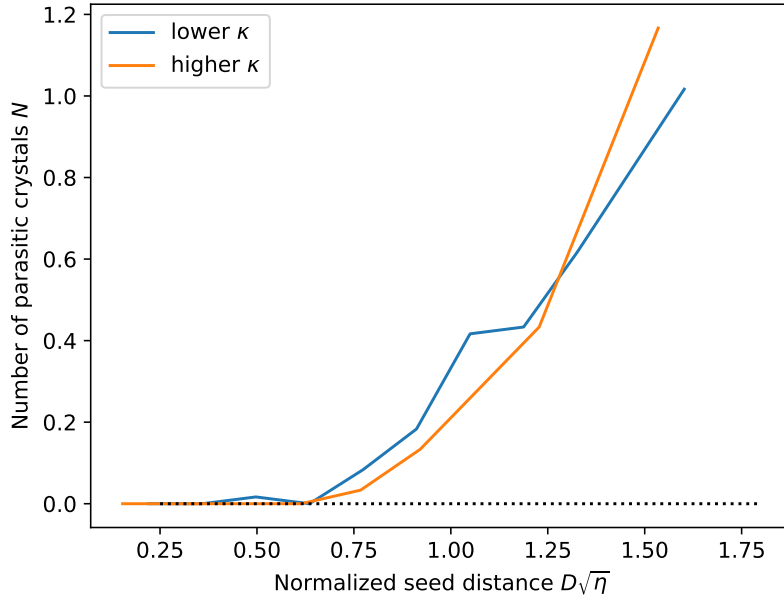


Figure S11: Evaluation of the number of parasitic grains for two different nucleation rates. Since the statistical errors for this process are rather large (see Figure 2, main text), the curves are equivalent, and therefore the ratio between growth and nucleation does not alter the result.

S2.6 Initial crystal size

The influence of the initial crystal sizes is investigated. To this end, two sets of simulations are conducted, varying the distances between the crystals and the crystal sizes. As shown in Figure S12, this size does not matter. The reason is as follows: the distance plotted on the x-axis represents the minimal distance between the surfaces of the crystals, which compensates for the shift in the graph resulting from varied initial crystal sizes.

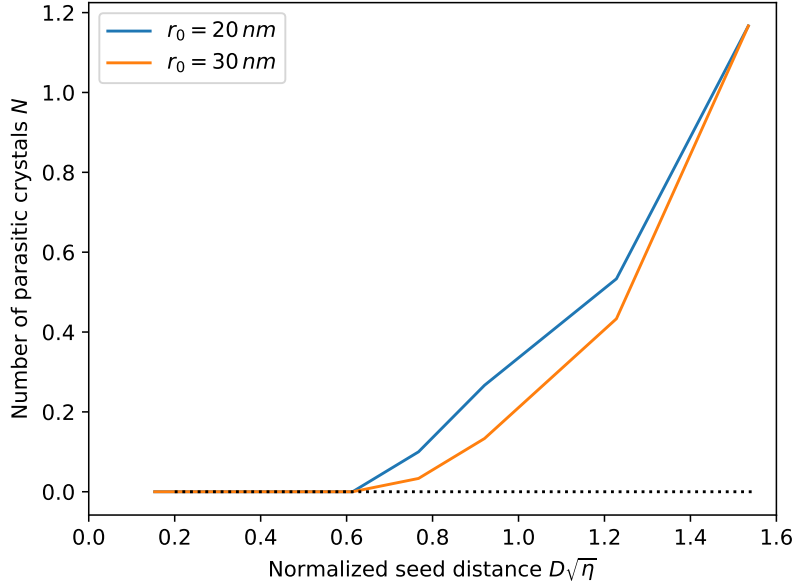


Figure S12: Evaluation of the number of parasitic grains for two different initial crystal sizes. Since the statistical errors for this process are rather large (see Figure 2, main text), the curves are equivalent, and therefore the initial crystal sizes do not alter the result.

S3 Analytical model

The experiment utilizes a triangular lattice of gold seeds, where the crystals preferentially nucleate. The dependence of the number of parasitic crystals on the pitch is investigated both numerically and analytically. For the analytical model, the crystal nucleation rate, crystal growth rate, and lag time of nucleation are required as input. These values can be evaluated from the simulations.

The setup is as follows: The area between three seeds is analyzed. The crystal center-to-center distance is called D . Therefore, the total area is

$$A = D^2/2, \quad (\text{S20})$$

The time until the crystals impinge on each other is

$$t < D/(2v_g). \quad (\text{S21})$$

It is assumed that crystals can nucleate anywhere within the amorphous phase with a rate of κ . In the simulation, crystals are placed on a triangular lattice. Since the size of the crystals does not matter (see Figure S12), we set the initial size of the crystals to zero in the model, hence:

$$A_c(t) = (v_g \cdot t)^2 \cdot \pi/2 \quad (\text{S22})$$

Each crystal is part of 6 unit cells in an infinite lattice. Therefore, each of the three circles in the triangle contributes 1/6 of its area.

Additionally, there is a nucleation induction time until the first crystal appears. This time is called t_0 . The total amount of parasitic grains N is therefore

$$N = \int_{t_0}^{D/2v_g} dt(A - A(t))\kappa. \quad (\text{S23})$$

Integrating yield:

$$N = \frac{\kappa D^3}{4v_g} \left(1 - \frac{\pi}{12}\right) + \frac{\kappa D^2 t_0}{2} \left(\frac{t_0^2 v_g^2}{3} - 1\right). \quad (\text{S24})$$

The simplifications used are:

- A lower limit is set for $t = D/v_g 2$, where the area in between the three impinging circles is still not crystalline.
- An upper limit is approximated with $t = 1.15D/v_g 2$, where all the material of the system is crystallized due to the growing seeds.
- The area covered by nucleated crystals is neglected, and hence, for long seed distances, it overestimates the number of parasitic grains.

S3.1 Analytical model - parameters

The input parameters to be set are the nucleation rate κ , the crystal growth rate v_g , and the nucleation induction time t_0 . The crystal growth rate v_g can be measured by simulating one growing crystal. We observe a value of $v_g = 142 \text{ nm/s}$ for the simulation parameters. For the nucleation rate κ and nucleation induction time t_0 , we use the same simulations, where η has been evaluated. We obtain a nucleation induction time of $t_0 = 0.1 \text{ s}$ and a nucleation rate of $\kappa = 2.1 \cdot 10^{-5} \text{ nm}^{-2} \text{ s}^{-1}$. The initial crystal size is set to 0 nm , but this value is not relevant for the results, as shown in Figure S12.

Evaluation of the nucleation rate and nucleation induction time

The nucleation rate and the nucleation induction time are evaluated from a simulation with no initially placed crystals. All further parameters are as stated above. Within the simulation, the nucleation induction time is defined as the time interval from $t = 0$ to the time at which the first crystal reaches the size of a critical germ. The number of crystals (larger than the critical germ size) and the amount of amorphous area are tracked. Its time derivative is scaled by the (time-dependent) amount of amorphous material to obtain the nucleation rate. This rate is averaged over time to obtain a constant value.

Crystal growth rate

The crystal growth rate is measured in a separate simulation, where a single crystal is placed within a box. Fluctuations increase the growth rate compared to the theory (simulations without fluctuations). Therefore, they are turned on. The area of the placed crystal is tracked until it impinges on newly nucleated crystals, and an equivalent radius of the circle is calculated. The growth rate is the time derivative of the radius's evolution.

S3.2 Calculating the nucleation density

According to the Johnson-Mehl-Avrami-Kolmogorow (JMAK) theory [31], the amorphous phase $A(t)$ in a system with homogeneously crystallizing crystals in 2D evolves as

$$\frac{A(t)}{A_{tot}} = \exp\left(-\frac{1}{3}\pi v_g^2 \kappa t^3\right), \quad (\text{S25})$$

where A_{tot} is the total area of the system, v_g the growth rate of the crystals and κ the nucleation rate. The nucleation density η can be calculated as

$$\eta = \frac{N}{A_{tot}} = \int_0^\infty dt A(t) \kappa, \quad (\text{S26})$$

where N is the total number of crystals in the system. Integrating numerically (with the nucleation and growth rate extracted from the simulation) yields $\eta_{num} \approx 2.7 \cdot 10^{13} \text{ m}^{-2}$. The value measured in the simulation ($\eta_{sim} \approx 2.2 \cdot 10^{13} \text{ m}^{-2}$) is substantially smaller. This is not unexpected, as JMAK considers only pairwise impingement and therefore overestimates the available area. Hence, we will use the simulated value for higher accuracy.

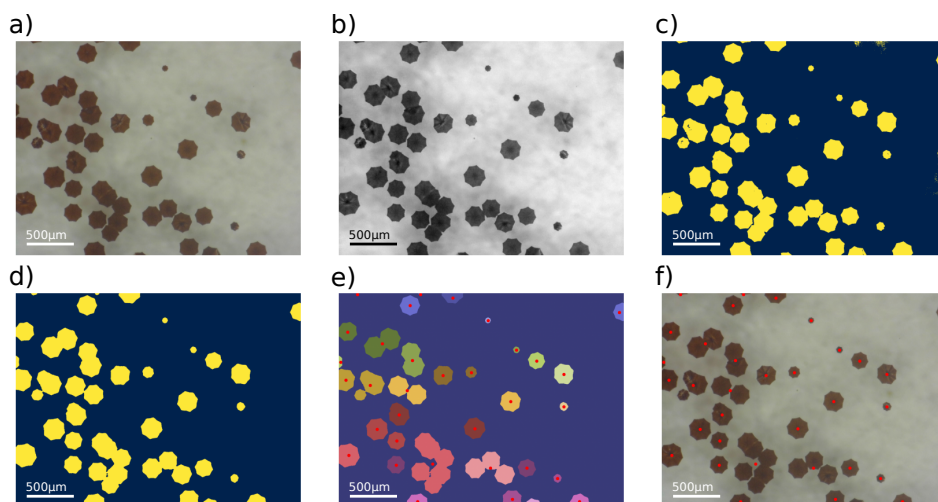


Figure S13: Example of the image processing done to determine the centroid points of all grains appearing in one in-situ image. The original image (a) is converted to greyscale (b). The resulting intensities are thresholded (c) to get a binary image. Opening and closing algorithms are used to get rid of artifacts occurring during thresholding (d). These binary regions are then analyzed (e) to determine the centroid points of each visible grain or grain cluster. The resulting centroids coincide with the grain centers, .i.e. with the nucleation point (f), provided the grain is relatively small and has not yet grown too far or fused with a neighboring grain.

S4 Sequential image analysis for the detection of the number of nucleating grains

The number of nucleation points per area is established via the image analysis of a sequence of microscope images acquired sequentially during grain growth by a camera placed above the sample. Each image is first analyzed to determine the centroid points of all grains or grain clusters appearing on the sample. Through a comparison of all centroid points appearing on one image to those on the next image, the true nucleation sites are then identified.

In Figure S13, the image processing done to each image is shown. The original image (Figure S13 a)) is first converted to greyscale values (Figure S13 b)). The resulting intensity values are then subjected to thresholding to separate the light background from the dark grains, resulting in a binary image (Figure S13 c)).

This binary image will usually still contain some artifacts: ideally, each grain will be a solid area of 'true' color values at this point, and the background will be solidly 'false'. Due to intensity variations on the grains and on the substrate, .i.e. due to light reflections, some pixels on the grains will appear too light to be correctly identified as 'true' and vice versa. To eliminate these artifacts, the image is opened, then closed at this point. Opening is a technique used in morphological processing to eliminate small areas below a critical radius, getting rid of noise on the substrate. Closing is the inverse and will fill in missing pixels in the otherwise solid grain regions. A resulting binary image is shown in Figure S13 d). In this image, connected regions of true pixels can be identified (Figure S13 e)). Their size and, crucially, their centroid location can be extracted. The centroid locations extracted this way from the original image are shown overlaid in Figure S13 f).

Analyzing the entire image sequence of grain growth, from the appearance of first nuclei until the substrate is fully covered, the location and number of true nucleation sites can now be determined. As clearly visible in Figure S14 a)-c), the processing of individual images yields the position of the centroid of each grain or grain cluster at that time. In the initial phase of grain growth, this

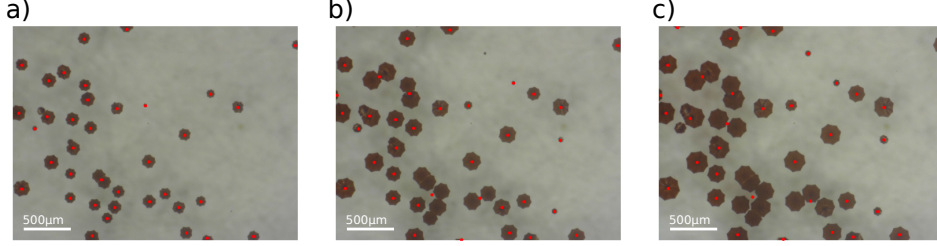


Figure S14: Series of images as they are recorded during grain growth with the identified centroid points. While some grains have not touched yet in (a) and generate their own centroid points, they will eventually meet as demonstrated in (b) and (c), resulting in joined centroid points that are not associated with an actual nucleation site.

point coincides with the nucleation site, as the grain is still small, grows relatively uniformly in all directions and has not yet fused with any neighboring grains. As the substrate is covered more and more fully, grains meet and fuse into larger regions, whose centroid locations do not correspond to any nucleation points anymore.

To identify the true nucleation sites, the centroid positions of each image are compared to those of the next sequentially. If a new centroid appears from one image to the next, the reason has the either be a newly nucleated grain, in which case this point can be noted as a nucleation center, or the meeting of two preexisting grains, which means the new centroid is to be ignored. Conversely, if a centroid disappears from one image to the next, we have to assume the corresponding grain has joined with a neighboring one. Upon the joining of two grains with areas A and B and centroids (x_A, y_A) and (x_B, y_B) , the new centroid coordinates will be given by:

$$x_{new} = \frac{x_A \cdot A + x_B \cdot B}{A + B}, \quad y_{new} = \frac{y_A \cdot A + y_B \cdot B}{A + B} \quad (\text{S27})$$

Therefore, to distinguish between 'real' new nucleation sites and 'false' new joined centroids, we can compare the coordinates of all disappeared old centroids and the areas of the corresponding regions to the coordinates of all new centroids. If two disappeared centroids can be attributed to a new one as described in Equation S27, the new coordinates can be discarded. Doing this for all images recorded, the true nucleation centers can thus be identified.

S5 Model Extensions

First, the shape of the patterning seeds may be changed, to reflect and investigate real achievable seeds and patterns. Second, the model could be extended to anisotropic growth mechanisms. As is visible in Fig. 6 (main text), the perovskite films under methylamine atmosphere exhibit preferred growth directions in accordance to the forming crystal lattice. Though this anisotropy is not sufficiently strong in this case to impact the findings from the model, an according extension of the model would be highly interesting for more anisotropic materials.

The analytic model and simulations could also be modified to include a third dimension. Under certain circumstances, there are gaps forming in between the final crystals in the experiment [9]. Especially for tight patterns or very slow growth speeds, material may run out before the next grain is met. The origin of this phenomenon would be an interesting starting point for further investigations. To reproduce this phenomenon we expect the simulations have to be more complex by including the third dimension. Additionally, a second material (air) may be necessary to allow for a free surface resulting in pinholes.

Furthermore, the simulations and model could be modified to describe a three dimensional system instead of the thin-film based 2D system presented here.

Experimentally, patterning systematically in three dimensions would be a challenging endeavor. While one could think of specific scenarios, i.e. inducing nucleation with a light intensity pattern, or mounting nucleation seeds on vertical structures, the experimental effort would be considerable. However, introducing artificial seeds as suspended particles during the fabrication of nanoparticles [32] or thin films [33] is established practice. Such a suspension acts as a statistical distribution of seeds with average distances, and as such could likely be modeled by a similar scheme.

References

- [1] Chuang Yang, Wenjing Hu, Jiale Liu, Chuanzhou Han, Qiaojiao Gao, Anyi Mei, Yinhua Zhou, Fengwan Guo, and Hongwei Han. Achievements, challenges, and future prospects for industrialization of perovskite solar cells. *Light: Science & Applications*, 13(1):227, 2024.
- [2] Jindan Zhang, Shicheng Tang, Mengqi Zhu, Zhenghong Li, Zhibin Cheng, Shengchang Xiang, and Zhangjing Zhang. The role of grain boundaries in organic–inorganic hybrid perovskite solar cells and its current enhancement strategies: A review. *Energy & Environmental Materials*, 7(4):e12696, 2024.
- [3] Chao Li and Cong Chen. Single-crystal perovskite for solar cell applications. *Small*, 20(48):2402759, 2024.
- [4] Zhongmin Zhou, Zaiwei Wang, Yuanyuan Zhou, Shuping Pang, Dong Wang, Hongxia Xu, Zhihong Liu, Nitin P. Padture, and Guanglei Cui. Methylamine-gas-induced defect-healing behavior of $\text{CH}_3\text{NH}_3\text{PbI}_3$ thin films for perovskite solar cells. *Angewandte Chemie International Edition*, 54(33):9705–9709, 2015.
- [5] Haochen Fan, Fengzhu Li, Pengcheng Wang, Zhenkun Gu, Jin-Hua Huang, Ke-Jian Jiang, Bo Guan, Lian-Ming Yang, Xueqin Zhou, and YanLin Song. Methylamine-assisted growth of uniaxial-oriented perovskite thin films with millimeter-sized grains. *Nature Communications*, 11(1):5402, 2020.
- [6] Daniel L. Jacobs and Ling Zang. Thermally induced recrystallization of MAPbI_3 perovskite under methylamine atmosphere: an approach to fabricating large uniform crystalline grains, supporting information. *Chemical Communications*, 52(71):10743–10746, 2016.
- [7] Emilia R. Schütz, Azhar Fakharuddin, Yenai Yalcinkaya, Efraín Ochoa-Martínez, Shanti Bijani, Abd. Rashid bin Mohd Yusoff, Maria Vasilopoulou, Tobias Seewald, Ullrich Steiner, Stefan A. L. Weber, and Lukas Schmidt-Mende. Reduced defect density in crystalline halide perovskite films via methylamine treatment for the application in photodetectors. *APL Materials*, 10(8):081110, 08 2022.
- [8] Thomas Geske, Junqiang Li, Matthew Worden, Xin Shan, Mingming Chen, Sri Ganesh R. Bade, and Zhibin Yu. Deterministic nucleation for halide perovskite thin films with large and uniform grains. *Advanced Functional Materials*, 27(40):1702180, 2017.
- [9] Antonio Günzler, Esteban Bermúdez-Ureña, Loreta A. Muscarella, Mario Ochoa, Efraín Ochoa-Martínez, Bruno Ehrler, Michael Saliba, and Ullrich Steiner. Shaping perovskites: In situ crystallization mechanism of rapid thermally annealed, prepatterned perovskite films. *ACS Applied Materials & Interfaces*, 13(5):6854–6863, 2021.
- [10] Rehan Kapadia, Zhibin Yu, Mark Hettick, Jingsan Xu, Maxwell S Zheng, Cheng-Ying Chen, Arunima D Balan, Daryl C Chrzan, and Ali Javey. Deterministic nucleation of InP on metal foils with the thin-film vapor–liquid–solid growth mode. *Chemistry of Materials*, 26(3):1340–1344, 2014.
- [11] Vaidotas Miseikis, Federica Bianco, Jérémy David, Mauro Gemmi, Vittorio Pellegrini, Marco Romagnoli, and Camilla Coletti. Deterministic patterned growth of high-mobility large-crystal graphene: a path towards wafer scale integration. *2D Materials*, 4(2):021004, 2017.
- [12] Mingzhan Wang, Jinxiong Wu, Li Lin, Yujing Liu, Bing Deng, Yunfan Guo, Yuanwei Lin, Tian Xie, Wenhui Dang, Yubing Zhou, et al. Chemically engineered substrates for patternable growth of two-dimensional chalcogenide crystals. *ACS Nano*, 10(11):10317–10323, 2016.

- [13] Xiaolong Xu, Yu Pan, Shuai Liu, Bo Han, Pingfan Gu, Siheng Li, Wanjin Xu, Yuxuan Peng, Zheng Han, Ji Chen, et al. Seeded 2d epitaxy of large-area single-crystal films of the van der waals semiconductor 2H MoTe₂. *Science*, 372(6538):195–200, 2021.
- [14] Liyang Yu, Muhammad R Niazi, Guy O Ngongang Ndjawa, Ruipeng Li, Ahmad R Kirmani, Rahim Munir, Ahmed H Balawi, Frédéric Laquai, and Aram Amassian. Programmable and coherent crystallization of semiconductors. *Science Advances*, 3(3):e1602462, 2017.
- [15] László Gránásy, Tamás Pusztai, and James A Warren. Modelling polycrystalline solidification using phase field theory. *Journal of Physics: Condensed Matter*, 16(41):R1205–R1235, 2004.
- [16] W. Wu, D. Montiel, J.E. Guyer, P.W. Voorhees, J.A. Warren, D. Wheeler, L. Gránásy, T. Pusztai, and O.G. Heinonen. Phase field benchmark problems for nucleation. *Computational Materials Science*, 193:110371, 2021.
- [17] James A. Warren, Tamás Pusztai, László Környei, and László Gránásy. Phase field approach to heterogeneous crystal nucleation in alloys. *Physical Review B*, 79(1), 2009.
- [18] C. Shen, J.P. Simmons, and Y. Wang. Effect of elastic interaction on nucleation: Ii. implementation of strain energy of nucleus formation in the phase field method. *Acta Materialia*, 55(4):1457–1466, 2007.
- [19] László Gránásy, Gyula I. Tóth, James A. Warren, Frigyes Podmaniczky, György Tegze, László Rátkai, and Tamás Pusztai. Phase-field modeling of crystal nucleation in undercooled liquids – a review. *Progress in Materials Science*, 106:100569, 2019.
- [20] Jesse L. Starger, Aaron T. Fafarman, Jason B. Baxter, Nicolas J. Alvarez, and Richard A. Cairncross. Quasi-2d model to predict solid microstructure in drying thin films. *Langmuir*, 39(46):16231–16243, 2023.
- [21] Martin Majewski, Shudi Qiu, Olivier Ronsin, Larry Lüer, Vincent Marc Le Corre, Tian Du, Christoph J. Brabec, Hans Joachim Egelhaaf, and Jens Harting. Simulation of perovskite thin layer crystallization with varying evaporation rates. *Materials Horizons*, 12:555–564, 2024.
- [22] Shudi Qiu, Martin Majewski, Lirong Dong, Andreas Distler, Chaohui Li, Karen Forberich, Jingjing Tian, Naveen Harindu Hemasiri, Chao Liu, Jiyun Zhang, Fu Yang, Vincent M. Le Corre, Max Bibrack, Robin Basu, Anastasia Barabash, Jens Harting, Olivier J. J. Ronsin, Tian Du, Hans-Joachim Egelhaaf, and Christoph J. Brabec. Over one-micron-thick void-free perovskite layers enable highly efficient and fully printed solar cells. *Energy & Environmental Science*, 18(12):5926–5939, 2025.
- [23] Olivier J. J. Ronsin and Jens Harting. Phase-field simulations of the morphology formation in evaporating crystalline multicomponent films. *Advanced Theory and Simulations*, 5(10):2200286, 2022.
- [24] Xi Yuan Feng, Kar Wei Ng, Shuang Peng Wang, Wen Zhou Chen, Zhen Zhong Zhang, Wei Chen, Yun Yang Zhao, Bao Tu, Zi Kang Tang, Hui Pan, and Zhu Bing He. Investigation on the role of amines in the liquefaction and recrystallization process of MAPbI₃ perovskite. *Journal of Materials Chemistry A*, 8(27):13585–13593, 2020.
- [25] Dmitry Bogachuk, Lukas Wagner, Simone Mastroianni, Michael Daub, Harald Hillebrecht, and Andreas Hinsch. The nature of the methylamine–MAPbI₃ complex: fundamentals of gas-induced perovskite liquefaction and crystallization. *Journal of Materials Chemistry A*, 8(19):9788–9796, 2020.
- [26] Kai Yan, Zhenda Lu, Hyun-Wook Lee, Feng Xiong, Po-Chun Hsu, Yuzhang Li, Jie Zhao, Steven Chu, and Yi Cui. Selective deposition and stable encapsulation of lithium through heterogeneous seeded growth. *Nature Energy*, 1(3):1–8, 2016.
- [27] Yuan Li, Shiqiang Hao, Jennifer G. DiStefano, Akshay A. Murthy, Eve D. Hanson, Yaobin Xu, Chris Wolverton, Xinqi Chen, and Vinayak P. Dravid. Site-specific positioning and patterning of MoS₂ monolayers: The role of au seeding. *ACS Nano*, 12(9):8970–8976, 2018.
- [28] Gang Hee Han, Nicholas J Kybert, Carl H Naylor, Bum Su Lee, Jinglei Ping, Joo Hee Park, Jisoo Kang, Si Young Lee, Young Hee Lee, Ritesh Agarwal, et al. Seeded growth of highly crystalline molybdenum disulphide monolayers at controlled locations. *Nature Communications*, 6(1):6128, 2015.

- [29] Gongming Wang, Dehui Li, Hung-Chieh Cheng, Yongjia Li, Chih-Yen Chen, Anxiang Yin, Zipeng Zhao, Zhaoyang Lin, Hao Wu, Qiyuan He, et al. Wafer-scale growth of large arrays of perovskite microplate crystals for functional electronics and optoelectronics. *Science Advances*, 1(9):e1500613, 2015.
- [30] John W. Mullin. *Crystallisation*. Butterworths, London, 2 edition, 1972.
- [31] Clinton DeW. Van Sice. Random nucleation and growth kinetics. *Physical Review B*, 54(17):11845–11848, 1996.
- [32] Meng-Qi He, Yongjian Ai, Wanting Hu, Liandi Guan, Mingyu Ding, and Qionglian Liang. Recent advances of seed-mediated growth of metal nanoparticles: from growth to applications. *Advanced Materials*, 35(46):2211915, 2023.
- [33] Yicheng Zhao, Hairen Tan, Haifeng Yuan, Zhenyu Yang, James Z. Fan, Junghwan Kim, Oleksandr Voznyy, Xiwen Gong, Li Na Quan, Chih Shan Tan, Johan Hofkens, Dapeng Yu, Qing Zhao, and Edward H. Sargent. Perovskite seeding growth of formamidinium-lead-iodide-based perovskites for efficient and stable solar cells. *Nature Communications*, 9(1):1607, 2018.